Light scattering by random shaped particles and consequences on measuring suspended sediments by laser diffraction

Y. C. Agrawal,[1] Amanda Whitmire,[2] Ole A. Mikkelsen,[1] and H. C. Pottsmith[1]

[1]   We present new observational data on small-angle light scattering properties of natural, random shaped particles, as contrasted with spherical particles. The interest in this "shape effect" on scattering arises from the need for a suitable kernel matrix for use in the laser diffraction method (LD) of particle sizing. LD is now used broadly for measuring size distribution of suspended marine particles. LD involves the measurement of small-angle forward scattering at multiple angles. This data is inverted using the kernel matrix to produce size distribution. In the absence of a suitable matrix for random shaped particles, past practice has been to use a model based on Mie theory, applicable strictly only to homogeneous spheres. The present work replaces Mie theory with empirical data. The work was motivated in part by anomalous field observations of size distribution and settling velocity distributions reported in literature. We show that a kernel matrix for random shaped particles results in improved interpretation of field multiangle scattering observations. In particular, a rising edge at the fine particle end of the size spectrum is shown to be associated with shape effects.

1.   Introduction

[2]   The size distribution and settling velocity distribution of particles are two fundamental properties of sediments that are central to studies of sediment transport. The development of instruments based on the principle of laser diffraction (LD) has made it possible to obtain such data in situ in various situations such as profiling, towed, or tripod-mounted use. Instruments of this type were described by *Bale and Morris* [1987] and *Agrawal and Pottsmith* [2000]. The latter of these instruments is now a commercial device under the name LISST-100 (Laser In-Situ Scattering and Transmissometry). There is now a growing body of literature on field measurements of size distribution with LISST-100 instruments. These instruments provide a 32-class size distribution. A version of this instrument with a settling column attachment, LISST-ST has also been in use for measurements of sediment settling velocity distribution in situ [*Thonon et al.*, 2005; *Pedocchi and Garcia*, 2006]. The LISST-100 instrument, although originally intended for sediment studies, is also in use for measuring inherent optical properties (IOPs) of water, namely, small-angle volume scattering function (VSF) and the beam attenuation coefficient [*Agrawal*, 2005; *Slade and Boss*, 2006]. It is this capability to measure the small angle volume scattering function that enables the present work, along with a newly devised, density-stratified settling column technique to sort random shaped particles by size, down to 2 microns. In the following, we describe first the principles of LD, followed by methods used in this work, and we end with the application of this new information on shape effects to field data, i.e., how it alters the interpretation of multiangle scattering into size distribution. The small-angle properties also impact derived estimates of settling velocities, however, that will be considered in a subsequent paper.

[3]   The motivation for the present work derives also from two frequent observations in field data. First, in the measurement of size distribution with LISST-100 instrument, a rising tail at the fine end of the size spectrum is often present [*Agrawal and Traykovski*, 2001; *Krishnappan*, 2000]. The rising tail can arise if particles are in suspension that are finer than the measurement range of the optics. In this case, these 'subrange' particles *leak* into the measured size spectra, and may produce a rising edge. The present work shows that the rising edge is also associated with shape effects, so that even when the 'subrange' particles may be missing, a rising edge becomes visible at the fine end of the size spectrum. The second motivating factor comes from estimates of settling velocity made with the related instrument, LISST-ST. This instrument, also for marine in situ use, employs a settling column in association with LISST-100. The settling column captures a sample of water and particles are allowed to settle over a 24-h period during which multiangle light scattering is measured at the bottom of the column at quasi-logarithmic time intervals. From these measurements of light scattering, the time

[1]Sequoia Scientific, Inc., Bellevue, Washington, USA.
[2]College of Oceanic and Atmospheric Sciences, Oregon State University, Corvallis, Oregon, USA.
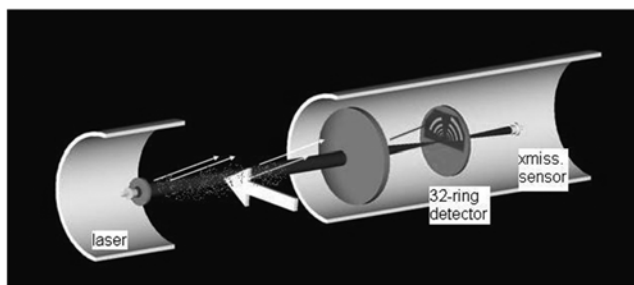
Figure 1. Optical schematic of the LISST-100 instrument used for present studies. Scattered light rays at any angle from the laser beam reach a point on the ring detector plane that subtends the same angle to the lens axis. A receiving lens focuses scattered light on to 32 ring detectors. The focused beam passes a 75-micron hole at center of ring detectors. A photodiode behind the ring detectors senses this beam power as a measure of beam attenuation.

history of size distribution is constructed over the settling duration. Typically, in this time history, the concentration of a particular size near the bottom of the settling tube remains steady for a time, and then as particles settle out, drops to zero. The time for settling is interpreted as a fall velocity or settling velocity. Settling velocity estimates by this method are offered only in 8 log-spaced size classes over a 200:1 size range, having to do with ensuring statistical independence [*Agrawal and Pottsmith*, 2000]. It is here that the second anomalous observation arises: the settling velocities of the finest 2 sizes exceed expected Stokes settling rates by an order of magnitude [*Pedocchi and Garcia*, 2006]. Although this could arise from these particles being of a particularly high mass density, this is not likely. *Pedocchi and Garcia* [2006] first suggested that particle shape effect

may explain this phenomenon. Thus, although not much sediment flux is usually associated with the finest sizes, an understanding of the anomaly is useful. Thus the motivation to understand shape effects is twofold: to explain a rising edge at the fine end of the size spectrum, and a faster-than-Stokes settling velocity estimated by the LISST-ST for the finest particles.

[4] To understand the principles of LD, consider light scattering by a particle as seen by the ring detectors shown in Figure 1. The scattering of light may be modeled as Fraunhofer diffraction [*Born and Wolf*, 1975] as was done originally when computational resources were limited [*Swithenbank et al.*, 1976], or, in modern times using Mie theory. The latter is a remarkably general theory, applicable to homogenous spheres of arbitrary size and refractive index, both without restrictions. Figure 2 shows the Mie result in intensity as a function of scattering angle θ [*van de Hulst*, 1981]. When this intensity is integrated over ring detectors (see Figure 1), that is when $\int \pi (i_1 + i_2) \sin\theta \, d\theta$ is computed, the scattering by a spherical particle takes the shape displayed as the broken line in Figure 2 (i_1 and i_2 are intensity functions [see *van de Hulst*, 1981]; θ is atan(r/f), r and f being, respectively, radius on the detector plane and receiving lens focal length; this value of θ is in air, in water, refraction reduces the angle by the ratio of refractive index of water and air, i.e., by 1.33). There are 32 ring detectors used in the LISST-100 instruments, hence the output of ring detectors is shown at 32 angles, corresponding to the center of each ring. From these 32 measurements, inversion yields concentration in 32 size classes, which is termed the size distribution. Note now that the dynamic range of the signature on ring detectors is much reduced. For this reason, this scattering signature is displayed on a linear ordinate. It is seen that the first lobe of Mie scattering of Figure 2
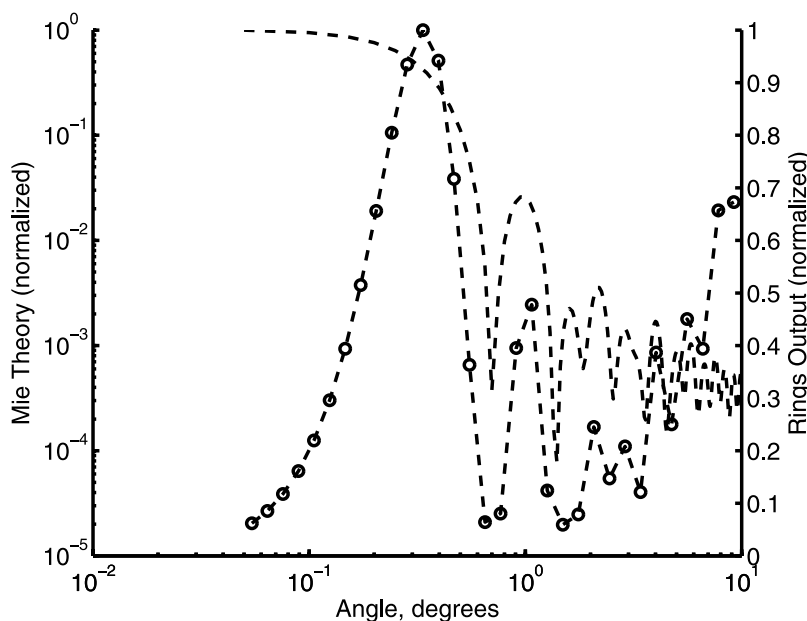

Figure 2. Mie calculations showing scattering versus angle from a spherical particle of radius 31.9 microns (solid line), normalized to its peak value. The broken line shows the same intensity distribution (normalized) as seen by the 32 ring detectors. The circles mark centers of ring detectors. Note the linear ordinate for ring output, implying a reduction in required dynamic range of measurement.

Figure 3. The four different particles studies in this work. (top left) From Satluj River, India; (top right) Paria river, Colorado, USA; (bottom left) aeolian particles provided by USGS; and (bottom right) ground coffee. The Satluj particles are most angular, and the aeolian particles are most rounded. Flakes in coffee grounds result from grinding, and could not be removed. Note the general absence of platy or elongated particles. PTI particles are similar to Paria river particles.

transforms to a first maximum across the ring detectors. The location and width of this principal peak derives from the width of the principal lobe of Mie theory, which depends solely on particle size. Subsequent peaks in Mie theory are smoothed out over logarithmically increasing widths of the ring detectors, transforming to weakening secondary maxima. An increase in size of the sphere narrows the Mie principal lobe of Figure 2, and consequently shifts the characteristic curve left, and vice versa (note the inverse relationship between particle size and location of principal maximum across rings). These principles are well known in LD literature [*Swithenbank et al.*, 1976].

[5] The net scattering from a suspension of a distribution of sizes is a weighted sum of the size distribution and the corresponding scattering for each size, written as a matrix product:

$$E = \underline{\underline{\mathbf{K}}}_{\mathbf{v}} \, \underline{V} \qquad (1)$$

where $\underline{E}$ is scattered optical power measured by the 32 ring detectors (units: watts), and $\underline{\underline{\mathbf{K}}}_{\mathbf{v}}$ is the kernel matrix. We use the subscript v for the kernel matrix $\underline{\underline{\mathbf{K}}}$ to indicate a matrix constructed per unit volume concentration of each size class of particles. The column vector $\underline{V}$ is the volume distribution, each element of which represents the volume concentration of a particular size class out of 32 classes (units: micro-liter/liter). The broken curve displayed in Figure 2 constitutes a

row vector in $\underline{\underline{\mathbf{K}}}_{\mathbf{v}}$; that is, it represents the scattering across ring detectors for unit concentration of particles of a particular size and refractive index. In an alternate formulation, the vector $\underline{E}$ may be set equal to a different matrix product, where the kernel matrix is constructed to invert for particle mass distribution, area distribution, or number distribution. In these cases, the kernel matrix is computed, respectively, per unit mass concentration, area concentration, or per particle. It is established in the literature [*Hirleman*, 1987] that the inversion of equation (1) to obtain the size distribution is most stable when logarithmically widening ring detectors are employed, and $\underline{E}$ is inverted for area distribution ($\underline{A}$) or volume distribution ($\underline{V}$) with the corresponding matrix $\underline{\underline{\mathbf{K}}}_{\mathbf{A}}$ or $\underline{\underline{\mathbf{K}}}_{\mathbf{v}}$. We employ the volume distribution throughout this paper.

[6] Owing to the broad applications to which the LD method has been adopted, interest in shape effects on this method is also quite old. The first significant results on shape effects were by *Shifrin et al.* [1984], *Jones* [1987], and *Al-Chalabi and Jones* [1994], who modeled random particles as random shaped apertures. This follows from the idea of diffraction. They predicted the diffraction as a function of increasing roughness of the aperture. Results showed that the deep minima of Mie theory became progressively shallower with increasing roughness. *Muhlenweg and Hirleman* [1998] also used a similar approach. Probably the most detailed shape-related calculations suitable for this method were performed by *Heffels et al.* [1996]. The shapes included rods, prisms, and crystalline shapes. The results were qualitatively similar to the diffraction part computed by *Jones* [1987], and *Al-Chalabi and Jones* [1994] in that both showed a weakening of the first and subsequent *minima* of Mie theory. However, in all these cases, no experimental data were offered to support the models. More advanced computational techniques such as the T-matrix approach and others surveyed in the text by *Mischenko et al.* [2000] have since been developed to compute light scattering by random shaped particles from fundamentals of optics. However, these methods are still impractical for an ensemble of real-world random shaped natural grains, particularly for large particles >10 μm. Remarkably, no laboratory data are available for random shaped, size-sorted particles. Only *Volten et al.* [2001] have considered natural samples, though not size-sorted and not at the needed small angles.

[7] Sedimentologists need to know how much mass of particles is present in a particular size class, containing particles between diameters d_1 to d_2 where the sizes are defined by sieving, or by settling rates. It is this need that drives the present work. For this, we need a kernel matrix $\underline{\underline{\mathbf{K}}}_{\mathbf{v}}$ of equation (1) for random shaped grains. Constructing $\underline{\underline{\mathbf{K}}}_{\mathbf{v}}$ for natural particles is our first object here.

[8] A clarification on the scope of this paper: The term 'random' refers to grains with no preferred axes; that is, elongated particles and platy particles are excluded from present consideration. For conceptual purposes, one may thus visualize a grain as a spherical surface with random bumps, scratches, and digs superimposed so that if an 'average shape' were constructed, it would still be a sphere. This clarification is important as there is specific interest in sedimentology as well as in optics in the scattering of light by elongated (ellipsoidal) or platy (planar) particles. All experimental data reported here were collected using

particle samples which showed no obvious preferred orientations (Figure 3).

2. Methods

[9] We have employed a LISST-100 type-C instrument in the present study. This instrument employs a 120-mm focal length receiving lens. The ring detectors have radii varying from 100 microns (innermost ring, inner radius) to 20 mm (outermost ring, outer radius) in 32 logarithmic steps, i.e., increasing by a factor 1.1809. Thus, the outer radius of any ring is 1.1809 times the inner radius. The inner radius of ring number n, r_n is:

$$r_n = 0.100 * 1.1809^{\wedge}(n-1) \text{mm}; 1 < n < 32 \qquad (2a)$$

The corresponding angles covered by ring n are determined by the 120 mm lens focal length as θ_n to θ_{n+1}, where

$$\theta_n = \text{atan}(r_n/120) \qquad (2b)$$

The 33 edges of 32 particle size classes, a_n are chosen from the relation [*Agrawal and Pottsmith*, 2000]:

$$ka_n \, \theta_{34-n} = 2; \; 1 < n < 33 \qquad (2c)$$

where k is $2\pi/\lambda$, and λ is wavelength of light in air. For this instrument, the angles range from 0.0477 degree to 9.46 degree; corresponding to the 32 particle size classes (also called size bins) spanning 2.58 to 511.8 microns. The middle of any size bin is taken as the geometric mean of its edges.

[10] We have sorted particles using sieves from 500 microns down to 16 microns, in 1/4 ϕ intervals. For the nonsedimentologist reader, a unit increase in ϕ represents a reduction in size by a factor of 2, so that the sieved bins are a factor, $2^{1/4} = 1.1892$ apart. These sizes, coincidentally, are within <1% of the sizes defined by equation (2c), which are a factor 1.18 apart, and were considered acceptably close to the sizes according to equation (2c), because, in any case, the resolution of the LD method is no better than a size bin. In all cases, dry sieving followed by wet sieving was performed for each size class until two successive sieved samples produced identical scattering measurements.

[11] The procedure to obtain characteristic scattering with the submersible LISST-100 is routine. A small mixing chamber provided by the manufacturer (Sequoia Scientific, Inc., Bellevue, Washington) was inserted in the optical path of the instrument and filled first with filtered water. A reading of ring detector outputs was stored. This constituted a background. Weighed samples of individual size bins were then sequentially suspended in the filtered water and the ring detector output was stored for each. The background was removed from the total scattering. Thus, the net scattering was obtained, from which molecular scattering of water and scattering of optical elements and windows had been removed. This procedure is described by *Agrawal and Pottsmith* [2000].

[12] Now a small aside. Any mixing chamber is characterized by a vertical gradient in concentration of particles. The gradient is established as a balance between gravitational settling and mixing, similar to sediment transporting marine boundary layers. The gradient can be minimized by vigorous mixing but stirring is sometimes limited by introduction of bubbles. For this reason, anticipating vertical gradients of sediment in the mixing chamber, for each size class we saved the net scattering normalized by the beam attenuation coefficient, c, which we call the characteristic scattering function (CSF) through out this paper. The beam attenuation coefficient in each experiment represents the concentration at the level of the laser, which is what is relevant to scattering by particles. Beam attenuation is measured accurately by the photodiode behind the ring detectors of the LISST-100 (Figure 1). The beam attenuation coefficient is extracted as:

$$c = -1/l \, \ln(\tau) \qquad (3)$$

where l is beam length in water (5 cm), and τ is the ratio of laser power sensed by the beam attenuation sensor with particles in water to its value with clean water.

[13] Along with random shaped particles, we also made measurements with glass spheres in some of the same size classes, sieved through the same sieves. This permits a relative view of the magnitude and shape of CSF of spheres and nonspheres. Further, a specific beam attenuation coefficient c_n was computed and saved for each size class of grains and spheres by normalizing the beam attenuation coefficient c with the mean mass concentration in the mixing chamber. This property, c_n (units: m^{-1}/mg-L^{-1}) will be shown in a composite figure including spheres and random shaped particles. Note that imperfect mixing will be reflected in these estimates of c_n. This summarizes the method for estimating the CSF for grains in the size range 16–500 microns.

[14] We next consider the CSF of particles smaller than 16 microns. These particles cannot be easily sorted by sieves. So, we resorted to sorting by settling columns. The use of settling columns for sorting particles is not new. But to sort particles that are in the few micron size range, particular care is required. For instance, Stokes settling velocity for glass spheres of 2 micron diameter is estimated as 3.5 microns per second. In order to avoid bias in measurements, it follows that residual convective motions in the settling column should be far weaker. We chose to achieve that by density stratifying the water column. The settling column was first attached to a LISST-ST instrument. We then filled the 30 cm tall settling column with a vertically increasing fraction of alcohol in water. This produced a decreasing density with increasing height, i.e., stable stratification (alcohol was used as it discourages flocculation). Particles, now suspended in pure alcohol, were inserted in a 3- to 5-mm thin layer at the top of the column. Particles then 'rained down' from the thin top layer into the stratified column and reached the laser beam 30 cm below, where multiangle scattering was recorded. The idea thus is to use settling time to define particle size using Stokes law, also corrected for shape effects.

[15] To relate settling time to grain size, we needed to estimate 2 additional unknowns: the effective viscosity of the settling column, and the departure from Stokes law due to random shape effect (change in settling velocity due to lower mass density of water-alcohol mixture varied from 0
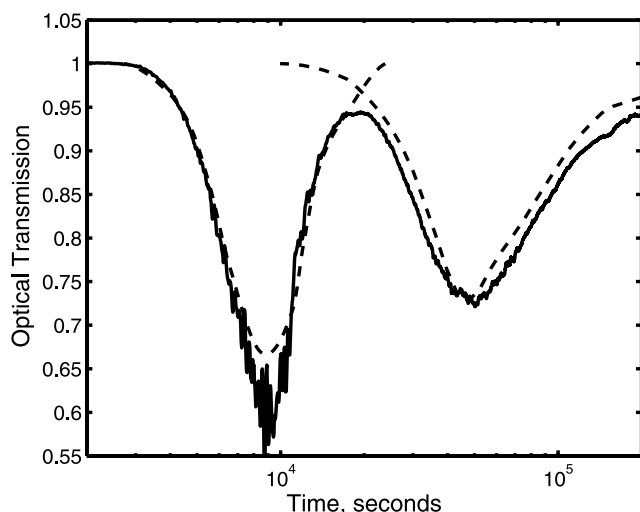
Figure 4. History of measured optical transmission in the settling column (solid line) compared with Stokes settling prediction of PTI particles (broken line).

to 3% and is ignored). Estimation of viscosity is relatively simple: known size glass beads were dropped through the column and their arrival time at 30 cm depth was estimated. Simple use of Stokes law then permitted estimate of the viscosity as 1.45 centi-stokes. In other words, settling was slower by a factor of 1.45 despite a tendency to increase settling velocity by up to 3% owing to lower fluid mass density. As an aside, we note the curious property of alcohol-water mixtures that with increasing alcohol concentration, the mixture viscosity first increases, before falling back down to the viscosity of pure alcohol. Mixture viscosity at 0, 25, 50, 75 and 100% alcohol is 1.02, 2.58, 3.08, 2.0, and 1.5 centi-stokes [*Weast*, 1977]. Our estimate of 1.45 seems reasonable.

[16] The second unknown, which is shape effect on settling velocity, required a different approach. In this case, we used a mixture of powders of 2 distinct size classes, nominally 2−6 and 6−11 microns, obtained from Particle Technology Inc.(PTI). A few milligrams of the mixture, again dispersed in pure alcohol, was inserted at the top of a freshly prepared stratified settling column. A record of the optical transmission at the bottom of the column was used to find the shape-related correction factor to Stokes law for spheres as follows.

[17] The underlying idea is that if the size distribution of particles is known, then assuming spherical shape and Stokes law, one can predict the beam attenuation record at the bottom of the settling column, 30 cm down. If shape of random grains causes a slowing compared to Stokes law, assuming it is by a fixed factor, the attenuation record will be delayed in time by the fixed factor. Thus, the task becomes to find this delay factor. For our work, the size distributions of the 2−6 and 6−11 micron powders were provided by PTI using a Coulter counter. These size distributions were manually digitized from the provided printouts, and converted to equivalent spheres area distributions. (Light attenuation is related to particle cross-section area, hence this step.) From the area distributions, i.e., area versus size of this mixture of two powders, and given the

30 cm column height, we predicted the optical transmission record assuming spheres of mass density 2.65 in water and a fixed extinction efficiency of 2. For each powder, we then found a factor such that when the predicted transmission record for it was delayed by this factor, prediction fitted observation. The delayed predicted record, and measured transmission records are shown in Figure 4. The delay factor, i.e., settling velocity reduction, for these fractions was respectively, 1.9 for the fine fraction and 1.75 for the coarse fraction, compared to equal diameter spheres settling in water. The ∼10% disparity for the two fractions is at least partly caused by the manual digitization of the PTI size distributions. We have chosen an average value of 1.83 to estimate the slowing of particles due to the combined effect of nonspherical shape and increased viscosity. Given that of this factor, 1.45 is due to viscosity, it follows that nonspherical shape for these particles produced a reduction in settling velocity by a factor of 1.83/1.45 = 1.2 ± 5%. This slowing due to shape is significant, and is contrasted with the factor 1.36 reported by *Dietrich* [1982] for larger particles. If particle shapes are geometrically similar for all sizes, this factor can be expected to be independent of size for these low Reynolds number situations. Microscope photos of particles did not reveal a noticeable difference in shape with size; however, it is difficult to be certain that particles had rigorously similar shapes. For this reason, we shall let the data speak for itself. Furthermore, it can be argued that any random particle has a preferred orientation since randomness of shape precludes symmetry of individual particles. Is this significant? The data presented next address findings.

[18] Having found the modified Stokes law applicable to these powders, to find the CSF of a particular size, one simply finds the settling time for that size (= 1.83 × Stokes settling time for spheres in water) and then looks at the measured multiangle scattering at that time. Again, in a manner similar to the procedure for coarse grains, we saved the CSF as the measured scattering normalized by the corresponding beam attenuation coefficient c. As noted, the normalization by c removes dependence on concentration. To construct a row of the kernel matrix, one needs the mean CSF for a size class. For this, we averaged the CSF during the particle settling interval corresponding to relevant edges of the size class.

[19] Returning briefly to Figure 4, the existence of twin minima in optical transmission, mirroring the size distribution of the inserted sample, is an indicator of the successful use of the stratified settling column. The clear separation of the transmission record into a coarse and fine mode suggests that formation of particle aggregates or the transport of fine particles in the wake of large ones was not significant. The continuing clearing of the water column at the end of the 2-d experiment further suggests that finer particles were still settling, unflocculated. In other words, our objective of unhindered, unflocculated settling in a still column appears to have been substantially met for particles as small as 2 microns. It follows that the density-stratified settling column suppressed convective motions to better than a few microns per second.

[20] We note also in passing, the method of smoothing of measured CSF employed with the fines in the settling column. As mentioned earlier, even random grains have
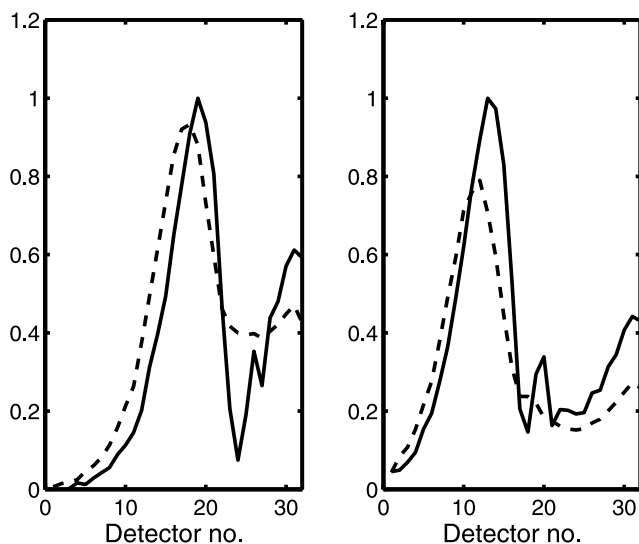
Figure 5. CSF of spheres (solid lines) and Satluj river particles (broken line) for two sizes; (left) 25–32 μm, (right) 75–90 μm; normalized to the peak value of CSF for spheres.

weakly preferred settling axes due to an absence of total symmetry. That leads to the acquisition of preferred orientation by particles falling in the settling column. The preferred orientation produces a weakly asymmetric scattering pattern on the ring detectors. In this case, the scattered light field shows a weak azimuthal variation in the plane of the ring detector. These variations appear as a weak sawtooth pattern in the angular scattering where the even numbered detectors may see slightly more light (~10%) than the odd numbered ones. Particles of all sizes showed the same, consistent sawtooth pattern (e.g., always the sawtooth patterns included higher light on odd numbered rings), independent of time, consistent with the idea of preferred orientation during settling. To remove the sawtooth shape of the measured scattering, the CSF was inverted using a kernel matrix for spheres, producing a volume distribution $\underline{V}$ as in equation (1). The fit, i.e., $\underline{\mathbf{K}}_\mathbf{v} \underline{V}$ was found to represent the desawtoothed characteristic scattering well. This procedure was found superior to a 2-point top hat running average. In this manner, we produced the CSF for sizes ranging from 2 to 16 microns.

[21] It is appropriate to note here that the CSF measurements have different basis for diameter definitions. The sieved fractions are defined on basis of sieve apertures, whereas the settling column particles are based on settling velocity. How consistent are these? We shall show a remarkable agreement between the two in Figure 7.

3. Results and Discussion

3.1. Light Scattering Properties of Natural Sediments and Spheres

3.1.1. Multiangle Scattering From Coarse Particles

[22] The first result we display is a comparison of the CSF of spheres, and natural grains from the Satluj river sample, sieved through identical sieves (Figure 5). To make the presentation of CSF more meaningful, we normalize the

two curves to the peak value of the CSF for spheres, so that the CSF for spheres has a peak of unity. As examples, two CSF's for sizes 25–32 microns and 75–90 microns are shown in Figure 5. It is evident that CSF of random grains differs both in magnitude and in location of the peaks. Natural grain scattering has a smaller, broader peak than spheres, and the peaks shift left, to smaller rings. As explained by *Agrawal and Pottsmith* [2000], shifts of 1 to 2 ring detectors implies an apparent size increase by one or two size classes, respectively. It was precisely this apparent increase in size that was reported by *Konert and Vandenberghe* [1997]. See also *Clavano et al.* [2007] for relevant theory for nonspherical but regular shaped particles.

[23] The CSF for 17 of 20 coarse sizes, each separated by 1/4 -ϕ, are displayed in Figure 6. The CSFs for the 3 largest sizes are not shown for clarity. In Figure 6, the smallest size fraction, corresponding to the extreme right peaking curve, is 16–20 microns. This size range corresponds to 0.33 ϕ; 1/4 -ϕ would be 16 to 19.02 microns. The reason is that sieves of precise sizes to get 1/4 ϕ spacing were not always available. The largest size fraction, corresponding to the extreme left peaking curve is 150 to 180 microns. Note that the finer fractions (curves peaking to the right) are smoother. At coarser particle sizes, mixing of particles remained a difficulty, and the data quality correspondingly suffered. Another notable fact is that the smallest angle, corresponding to ring detector no.1, is 0.048-degree. At this small angle, alignment of the laser to the axis of the concentric detectors is extremely critical. Imperfect alignment explains some of the imperfection in the shape of the CSF curves of Figure 6.

[24] The data of Figure 6 show (1) a tendency to a common value of peak for the CSF's, similar to the property of spheres according to Mie theory; (2) a weak, but faintly discernible second maximum which, in contrast, is
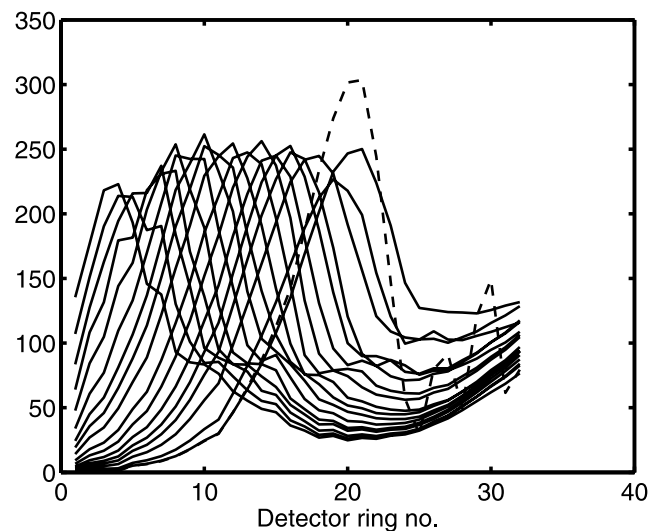

Figure 6. The raw CSF of size-sorted random shaped grains from the sieved set, before smoothing. Each curve shows the CSF of a particular narrow-size class from the set. For reference, a single curve for a narrow class spheres (25–32 microns) is shown (tallest curve). Ordinate is digital counts.
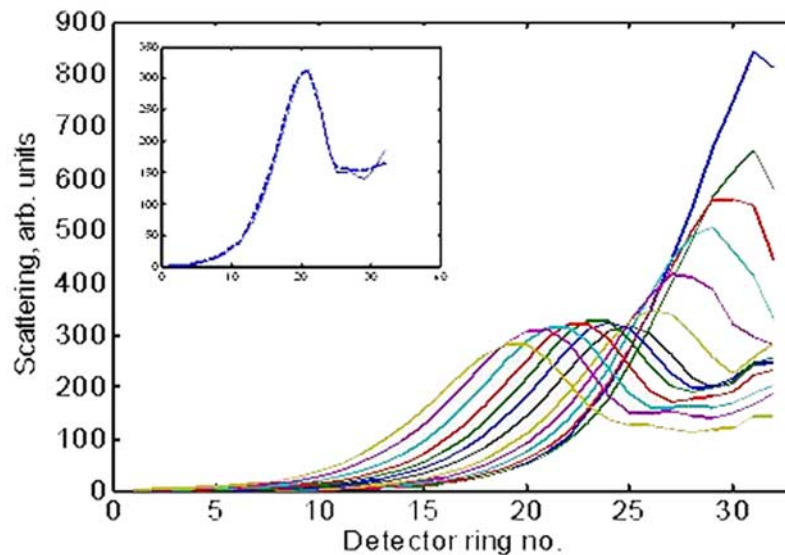
Figure 7. CSF for the fine particle size classes; data from settling column tests. This set covers particle sizes of 16 microns and smaller. Inset (axes same as main figure) shows a comparison of CSF of $16-20$ micron particles as measured from the settling column tests (solid line) and from sieving (broken line).

well-defined for spheres, (3) a common shape for all curves to the left of the main peak, which is the diffraction region; (4) a tendency, with increasing size, for a deepening of the first minimum of CSF to the right of the main peak, and (5) a tendency for the tails at outer rings to reach a common value. The last of these properties is known, for spheres, to arise from the fact that the large-angle part of CSF curves follows geometric optics. The separation of forward scattering into a diffraction part at the smallest angles, i.e., the principal lobe of Figure 2, and a refracted part at larger angles was formally shown by *van de Hulst* [1981, p. 209]. The refracted part, i.e., light that went through the particle, follows geometric optics for sufficiently large particles. In geometric optics, scattering is proportional to particle area, as also is beam extinction, so that they cancel out in calculating the CSF, and CSF becomes independent of particle size. In other words, the tails of CSF for large particles reach common values for all sufficiently large spherical particles. Given the irregular shape of the random particle surface, it is not immediately obvious that random shaped particles would refract light similarly to spheres, producing similarly common values for tails of CSF. Apparently, a similar result does apply for these random shaped particles also, as evident in Figure 6.

3.1.2. Multiangle Scattering From Fine Particles: Settling Column Data

[25] In Figure 7, we show the characteristic scattering functions for the 12 finest size classes, beginning with $2.5-2.97$ microns, and increasing successively by the factor $2^{1/4}$. These curves represent the averaged CSF for particles within each size class, i.e., averaged over all scans that correspond to the fall times of the particles within the size class. Also included in the inset is a comparison of the CSF of an overlapping size, where measurements in the settling column, and from sieved particles were both available. The two methods produce

near-identical CSF, which validates agreement between the two sizing methods (sieving and settling), and the smoothing procedure described in section 2.

[26] Before synthesizing the CSF measured by the two methods into a CSF for the entire size range of interest, we note that (1) Figure 7 reveals an increasing amplitude for 4 smallest sizes; and (2) for decreasing sizes, the first minimum following the main diffraction peak weakens in significance. This diminishing minimum appears to be a continuation of the pattern that can be seen with coarse particles (Figure 6).

3.1.3. Synthesis of Coarse and Fine Particle CSF to Form Kernel Matrix

[27] To construct the matrix $\underline{\underline{\mathbf{K}}}_V$ of equation (1) for these natural particles, we set the 32 rows of the matrix to the respective CSFs. Barring the smallest 4 sizes, which show a tendency for increasing magnitudes, the magnitudes of the CSFs for the different size fractions, which were noted to be nearly equal (Figures 6 and 7) were formally equalized. This permitted the construction of the matrix $\underline{\underline{\mathbf{K}}}_c$ where we now use the subscript **c** for the moment to retain the idea that this matrix is based on CSF. In other words, instead of a row of the matrix representing light scattering per micro-liter/liter or mg/liter of sediment, it represents light scattering per m^{-1} attenuation. To go from $\underline{\underline{\mathbf{K}}}_c$ to $\underline{\underline{\mathbf{K}}}_V$ requires a relation between size and attenuation per unit mass concentration and the mass density. We discuss this next.

[28] The beam attenuation properties of glass spheres and random shaped grains are displayed in Figure 8. These data are from the same experiments that produced the CSF for the sieved fractions, i.e., from fractions that are $1/4$ -ϕ wide, spanning 16 to 500 microns. In addition, we have inserted data for 3 PTI powders, which contained particles in $2-6$, $4-8$, and $6-11$ micron sizes. For large spherical particles, and also for large nonspherical particles with average cross-sectional area replacing cross-sectional area where extinc-
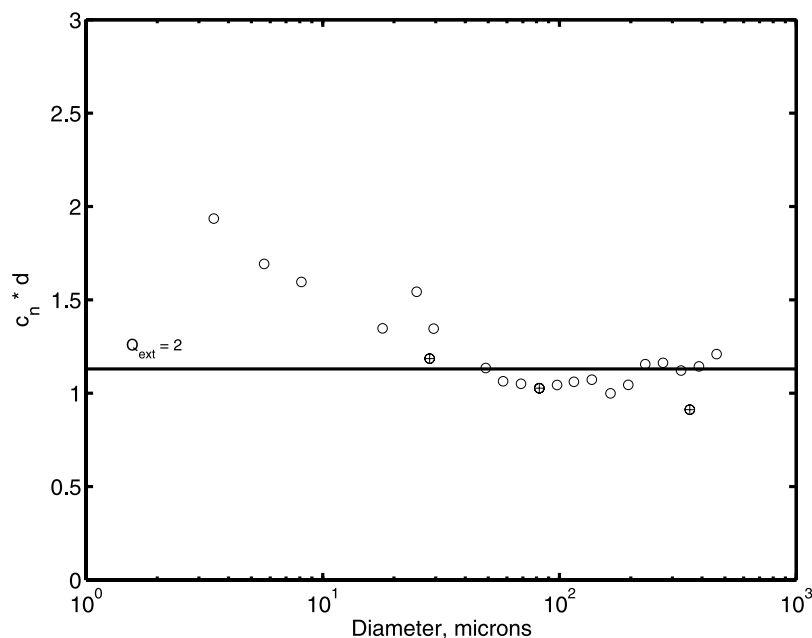
Figure 8. Comparison of measured extinction efficiency of random shaped (circles) and spherical (pluses) particles per unit mass concentration, shown multiplied by diameter. The line corresponding with large particle limit of Mie theory, where extinction efficiency $Q_{ext} = 2$ is also shown for comparison. Data for the three smallest sizes are from PTI powders; all others are from sieved fractions.

tion efficiency Q_{ext} of particles reaches 2 [*Clavano et al.*, 2007; *Mischenko et al.*, 2000], one can derive a relationship between beam extinction coefficient and diameter from:

$$c_n = Q_{ext}(\pi\, a^2)/\left[\frac{4}{3}\,\pi\, a^3 \rho\right];\ \text{or}$$

$$c_n = 1.13\ d^{-1}\,\mathrm{m}^{-1}(\mathrm{mg/L})^{-1};\ d\ \text{in microns.}$$

(4)

In order to exhibit changes from the ideal extinction value of 2, in Figure 8 we show the product $d*c_n$ along with a line corresponding to an extinction efficiency of 2. Particles larger than 30 microns fit equation (4) within 5%. The attenuation coefficient of glass spheres, also included in this data (+) are indistinguishable from grains. At the fine particle end, the attenuation coefficient seems to exceed $Q_{ext} = 2$, as is also known for spheres from Mie theory. More detailed study of this region of particle sizes is clearly warranted. This completes the description of the attenuation coefficient per unit mass of particles, c_n. so that we can proceed to converting the Kernel matrix $\underline{\underline{K_c}}$ which is constructed per unit attenuation coefficient, to per unit mass, or per unit volume concentration $\underline{\underline{K_v}}$.: Each row of the matrix $\underline{\underline{K_c}}$ is multiplied by the specific beam attenuation coefficient for the corresponding size. For sizes greater than 30 microns, c_n is estimated from equation (4). For smaller sizes, we use c_n as measured and shown in Figure 8. For example, row 1 of the matrix, representing size class 1, is multiplied by a value of c_n for size 1, etc. The entire matrix is then multiplied by the mass density 2.65 to go from a kernel matrix that is per unit mass, to per unit volume concentration, i.e., $\mu L\ L^{-1}$. This matrix is shown in Figure 9 (left), and it illustrates the differences with the corresponding matrix for spheres (Figure 9, right). It is noteworthy that the maxima of the natural particle matrix shift monotoni-

cally with size. In mathematical terms, the maxima lie on the diagonal of the kernel matrix, which makes the kernel matrix well-conditioned, and which permits stable inversion of equation (1) to construct the size distribution $\underline{V}$. This concludes the construction of the kernel matrix $\underline{\underline{K_v}}$ for grains.

3.1.4. Variability of CSF for Particles From Different Sources

[29] In order for field observations of multiangle scattering to benefit from the knowledge of shape effects, it is important to study variability in the CSF for particles of different origins. In other words, is it possible to construct
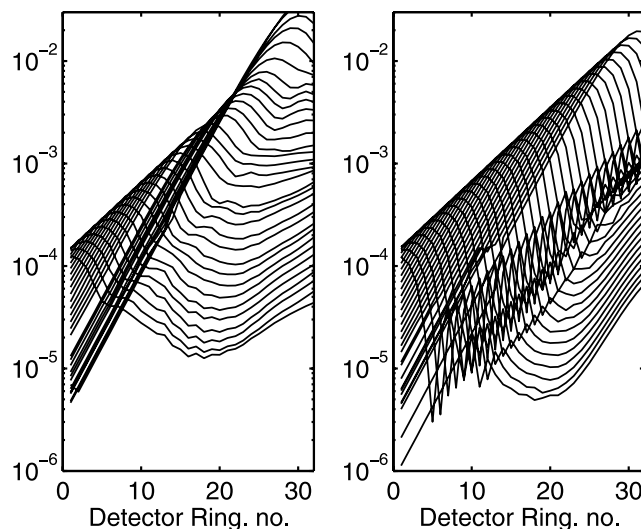

Figure 9. Kernel matrix (left) as formed from present work for natural particles; and (right) for spheres. Each curve is a row of the kernel matrix $\underline{\underline{K_v}}$.
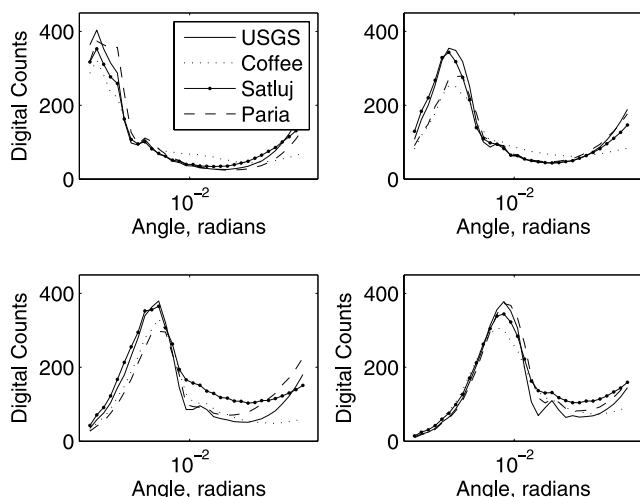
Figure 10. Variability of scattering for a particular size fraction from four distinct sources of particles. Ordinates are digital counts. Note the consistently distinct signature of absorbing particles (coffee). The rounded Aeolian particles even produce a clear second maximum, similar to spheres (bottom right). Size ranges for these plots are: left to right, top to bottom: 250–300, 125–150, 63–75, and 32–38 μm. Ordinate is digital counts.

a single matrix such as the one that we have, and apply it to field data from different places with the a priori knowledge that some of the constraints (absence of platy particles) are met.

[30] In Figure 10 we show the CSF for the 4 types of particles: an Aeolian sample provided by USGS (labeled USGS), sediments from the Satluj river in Indian Himalayas, from the Paria river which is a tributary to the Colorado river below the Glen Canyon dam in Arizona, USA, and coffee grounds. Photos of these grains were shown in Figure 3. Satluj river particles were the most angular, the Paria river particles less so, the USGS particles were rounded, and coffee grounds were rough and dark, with inclusion of a small amount of flakes from the coffee grinding process. The data presented are for 4 distinct coarse sizes, again sorted by sieving.

[31] What is similar for all the particles is the location of the primary peak in the CSF. It can be seen that for all particles, the main peak does not move by even one detector. This implies that their apparent size would also

differ less than one size class. The coffee grains do show a weaker peak, however. Thus, measuring dark grains with a matrix such as we have constructed will underestimate the concentration alone, by an amount equal to the ratio of the peaks, i.e., about 10%, while still recovering the correct size. The second maximum in CSF, that is well-defined for spheres, is barely perceptible for all but the rounded Aeolian particles in these data. Thus, rounded but random shaped particles do appear similar to spheres, particularly for the smallest of the sizes shown here, 32–38 μm. Remarkably, and fortunately, the scattering patterns of all sizes beyond the main peak are very similar. This implies that the differences in light scattering by particles from different sources are smaller than the differences between any random particle and a sphere. This finding further assures us of the validity of using a random particle matrix to analyze natural sediment data.

[32] The case of highly absorbing particles stands out in these data. Scattering by coffee grounds beyond the main peak differs in shape and magnitude when compared to the other grains. Specifically, the scattering by coffee grains lacks structure, and is lower in magnitude beyond the main diffraction peak. The lower magnitude follows from the fact that beyond the main diffraction peak, refracted light is a significant contributor to the total scattering strength, and the refracted light, having transited the particle, is diminished by absorption. Inverting data from highly absorbing particles with a matrix constructed for weakly absorbing particles will result in some errors, generally underestimating concentration.

[33] To conclude, it appears that, not surprisingly, there is a continuum of change from spheres to random particles. Rounded random shapes retain a defined second peak, which disappears with the rougher grains. Particles that differ in roughness appear more similar among themselves than they do to spheres. The highly absorbing particles scatter less light beyond the main diffraction lobe. In other words, some prior knowledge of the degree of absorption of the particles would be helpful in improving the inversion. It follows that laser wavelength that is only weakly absorbed (e.g., red) would have smaller errors than one that is strongly absorbed (e.g., green).

3.2. Application of Measured Properties to Laboratory and Field Data

[34] In order to understand the consequence of shape effect on inversions, we display the equivalent spheres size
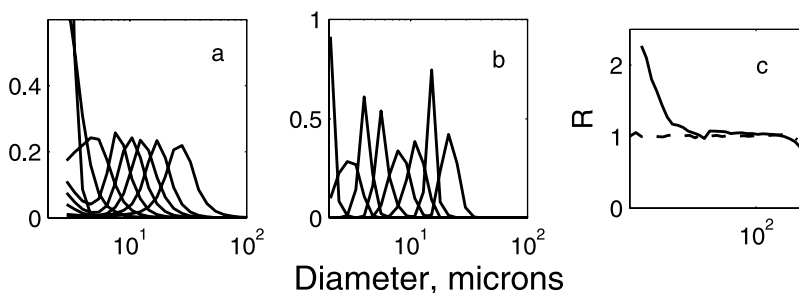

Figure 11. The (a) equivalent-spheres size distribution and (b) equivalent-grains size distribution of sediment grains in size classes 1:2:16. Note the rising edge on the small size end for equivalent spheres. (c) The ratio of apparent to true concentration of grains for equivalent spheres (solid line) and grains inversions (broken line).
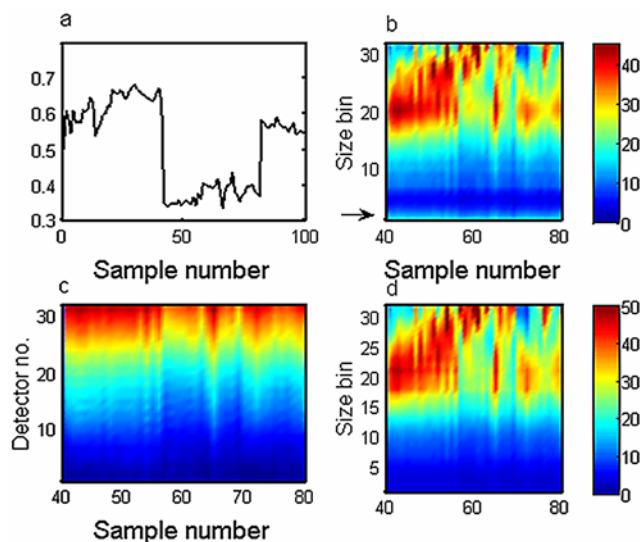
Figure 12. Suspended particles seen as equivalent spheres or random grains. (a) A section of the optical transmission record (the dip) is shown in detail. (b) Equivalent spheres size distribution; (c) The light scattering on detectors (units: digital counts; magnitudes are $100\times$ values on color bar), and (d) natural grain size distributions. The color bars for Figures 12b and 12d show concentration in mg/L. Note the dip (dark band) followed by a rising edge at small size bins in Figure 12b, marked by arrow; it disappears in the inversion for grains (Figure 12d).

distribution for each of the grains in the finest size classes, from 1 to 16. This is done using the standard software for inversion of scattering data as provided by the manufacturer of LISST-100 (Sequoia Scientific, Inc.). For each size class, a corresponding row of the kernel matrix $\underline{\underline{K}}_v$ for random particles is used as data vector $\underline{E}$. Each of the natural particle size classes thus results in an equivalent sphere size distribution. This is displayed in Figure 11a. It is clear that natural particles *invent* fine spherical particles. The invented fines are most pronounced for the smallest sizes. In contrast, the size distribution obtained by inversion using the natural particle matrix, Figure 11b shows no such invention, or rising tails. The apparent concentration for the equivalent spheres and random shape inversions is obtained by summing area under each curve (Figures 11a and 11b). This is displayed in Figure 11c, which shows that concentration is overestimated for the finer fractions with equivalent sphere inversion, not so with inversion for grains. The implication is clear: when fine natural particles are present in suspension, the equivalent spheres inversion invents particles that create the rising edge at the fine particle end. The reader will recall that this observation was a motivating factor for the present study.

[35] We next contrast size distributions as equivalent spheres and as natural grains from a field experiment. The experiment was carried out off the coast of California, next to the pier at Santa Cruz in about 10 m of water [*Thorne et al.*, 2007]. In order to study vertical gradients in sediments, a suite of instruments that contained 2 vertically separated LISST-100s was deployed on a bottom-mounted tripod, with the lower instrument at 0.8 m above bottom and upper

instrument at 1.6 m. The data presented here are from the lower instrument. The instruments were deployed on 03 March 2003. A 40-sample burst at 2 s sampling interval was acquired each half hour. The deployment period saw the passage of a major storm event on 16 March. The data presented here are from a burst of data captured beginning 05:01:25 h during this storm event.

[36] Figure 12a shows the optical transmission measured by the LISST spanning the event. The burst of interest is the 40-sample dip in optical transmission in the middle, beginning at sample 41 and ending at 80. The corrected net scattering for the burst is displayed in Figure 12b. The computed equivalent spheres size distribution is displayed in Figure 12c and below it, for easy alignment by eye, is the grains inverse. An arrow at Figure 12c marks a rising edge at the smallest size bin (ordinate value of 1). Between size bins 1 and 6, there is a minimum (a dark band). A similar rising edge was noticeable in a Coastal experiment, reported by *Agrawal and Traykovski* [2001]. In Figure 12d, the size distribution constructed for random grains removes this rising edge, showing a steady decline in size distribution left of the main peak. This example shows how the equivalent sphere inversion 'invented' fines, while the real reason for the rising edge was the difference in light scattering properties of natural grains.

4. Conclusions

[37] The data presented in this work complement the work of *Konert and Vandenberghe* [1997]. Whereas they concerned themselves with how random shaped coarse grains are seen when viewed as equivalent spheres, we have addressed the question: why are they seen this way, i.e., what differences in light scattering properties between spheres and random grains explain this apparent difference. The experimental work involved two difficulties: one of producing uncontaminated sieved samples, and the other of creating a convection-free settling column. Neither of these methods was straightforward. A reader inspired to repeat the work should take care to sieve carefully so that no fine particles cling to coarse ones. In this case, wet sieving with water and alcohol is helpful. The settling column work, on the other hand, required careful attention to selecting methods for column formation, particle insertion, and trial and error to determine concentrations of inserted samples so that particle-particle interaction remained insignificant. These methods in themselves are valuable in studying other types of particles in future work.

[38] While we are focused on finding differences in light scattering by spheres and random natural particles, we first note the similarities. The principal maximum for spheres, which is located at a particular angle (detector ring) for a given size remains nearly in the same place for random shaped particles, displaced $\sim$1 detector to the left. Thus natural grains appear about $1/4$ ϕ larger as equivalent spheres. The smallness of this shift is significant as it lends validation to historical and widespread practice of using the laser diffraction method for nonspheres such as in cements, pharmaceutical industries, and in laboratories concerned with particles in general.

[39] As for differences in the light scattering properties between spheres and random shaped grains, we have

reported 3. These are: (1) a shift in the scattering pattern across the ring detectors by approximately one detector ring, which corresponds to an apparent one size class larger equivalent spheres size, (2) the absence or weakening of secondary maxima on scattering patterns across the ring detectors; and (3) a progressive weakening of the first minimum beyond the diffraction peak, with decreasing particle size. The weakening minimum in the shape of the scattering with decreasing grain size is a key new finding. It helps explain the spike on the fine particle end of the size spectrum previously reported in nature.

[40] Our limited view of light scattering by random particles from varying sources has shown small variations between them. Smooth, rounded but random shaped particles tend to behave a bit like spheres. Highly absorbing grains are recognizably different in their scattering signature at the larger angles than nonabsorbing particles. River sediments from two vastly different sources showed insignificant differences. Thus, the laser diffraction method is generally consistent with all particles, but a user should be aware of these minor deviations.

[41] Finally, with the availability of a 'natural particle kernel matrix', examination of vertical gradients in particle populations in a boundary layer may now become possible. Prior examination of vertical gradient in the context of the Rouse profile by one of the authors (Y. Agrawal) has been unsuccessful. We shall report results in future publications.

References

Agrawal, Y. C. (2005), The optical volume scattering function: Temporal and vertical variability in the water column off the New Jersey coast, *Limnol. Oceanogr.*, *50*, 1787–1794.

Agrawal, Y. C., and H. C. Pottsmith (2000), Instruments for particle size and settling velocity observations in sediment transport, *Mar. Geol.*, *168*, 89–114, doi:10.1016/S0025-3227(00)00044-X.

Agrawal, Y. C., and P. Traykovski (2001), Particles in the bottom boundary layer: Concentration and size dynamics through events, *J. Geophys. Res.*, *106*, 9533–9542, doi:10.1029/2000JC900160.

Al-Chalabi, S. A. M., and A. R. Jones (1994), Development of a mathematical model for light scattering by statistically irregular particles, *Part. Part. Syst. Charact.*, *11*, 200–206, doi:10.1002/ppsc.19940110306.

Bale, A. J., and A. W. Morris (1987), In situ measurement of particle size in estuarine waters, *Estuarine Coastal Shelf Sci.*, *24*, 253–263, doi:10.1016/0272-7714(87)90068-0.

Born, M., and E. Wolf (1975), *Principles of Optics*, 808 pp., Pergamon, New York.

Clavano, W. R., et al. (2007), Inherent optical properties of non-spherical marine-like particles—From theory to observations, in *Oceanography and Marine Biology: An Annual Review*, vol. 45, edited by R. N. Gibson et al., pp. 1–38, CRC Press, Boca Raton, Fla.

Dietrich, W. E. (1982), Settling velocity of natural particles, *Water Resour. Res.*, *18*, 1615–1626, doi:10.1029/WR018i006p01615.

Heffels, C., P. J. T. Verheijen, D. Heitzmann, and B. Scarlett (1996), Correction of the effect of particle shape on the size distribution measured with a laser diffraction instrument, *Part. Part. Syst. Charact.*, *13*, 271–279, doi:10.1002/ppsc.19960130504.

Hirleman, E. D. (1987), Optimal scaling of the inverse Fraunhofer diffraction particle sizing problem: The linear system produced by quadrature, *Part. Part. Syst. Charact.*, *4*, 128–133, doi:10.1002/ppsc.19870040127.

Jones, A. R. (1987), Fraunhofer diffraction by random irregular particles, *Part. Part. Syst. Charact.*, *4*, 123–127, doi:10.1002/ppsc.19870040126.

Konert, M., and J. Vandenberghe (1997), Comparison of laser grain size analysis with pipette and sieve analysis: A solution for the underestimation of the clay fraction, *Sedimentology*, *44*, 523–535, doi:10.1046/j.1365-3091.1997.d01-38.x.

Krishnappan, B. G. (2000), In situ size distribution of suspended particles in the Fraser River, *J. Hydraul. Eng.*, *126*, 561–569, doi:10.1061/(ASCE)0733-9429(2000)126:8(561).

Mischenko, I. M., J. W. Hovenier, and L. D. Travis (2000), *Light Scattering by Non-Spherical Particles*, 690 pp., Academic Press, San Diego, Calif.

Muhlenweg, H., and E. D. Hirleman (1998), Laser diffraction spectroscopy: Influence of particle shape and a sharp adaptation technique, *Part. Part. Syst. Charact.*, *15*, 163–169, doi:10.1002/(SICI)1521-4117(199808)15:4<163::AID-PPSC163>3.0.CO;2-8.

Pedocchi, F., and M. H. Garcia (2006), Evaluation of the LISST-ST instrument for suspended particle size distribution and settling velocity measurements, *Cont. Shelf Res.*, *26*, 943–958, doi:10.1016/j.csr.2006.03.006.

Shifrin, K. S., et al. (1984), Light scattering by an ensemble of large particles of arbitrary shape, (in Russian), *Dokl. Akad. Nauk SSSR*, *277*, 582–585.

Slade, W. H., and E. S. Boss (2006), Calibrated near-forward volume scattering function obtained from the LISST particle sizer, *Opt. Express*, *14*, 3602–3614, doi:10.1364/OE.14.003602.

Swithenbank, J., et al. (1976), A laser diagnostic technique for the measurement of droplet and particle size distribution, in *Experimental Diagnostics in Gas Phase Combustion Systems*, *Prog. Astron. Aeron.*, vol. 53, edited by B. Zinn, pp. 76–79, Am. Inst. of Aeron. and Astron., New York.

Thonon, I., et al. (2005), In situ measurements of sediment settling characteristics in flood plains using a LISST-ST, *Earth Surf. Processes Landforms*, *30*, 1327–1343, doi:10.1002/esp.1239.

Thorne, P. D., et al. (2007), A comparison of acoustic backscatter and laser diffraction measurements of suspended sediments, *IEEE J. Oceanic Eng.*, *32*, 225–235, doi:10.1109/JOE.2007.890978.

van de Hulst, H. C. (1981), *Light Scattering by Small Particles*, 470 pp., Dover, Mineola, N. Y.

Volten, H., et al. (2001), Scattering matrices of mineral aerosol particles, *J. Geophys. Res.*, *106*, 17,375–17,401, doi:10.1029/2001JD900068.

Weast, R. C. (1977), *CRC Handbook of Chemistry and Physics*, 58th ed., CRC Press, Boca Raton, Fla.

―――――――――――

Y. C. Agrawal, O. A. Mikkelsen, and H. C. Pottsmith, Sequoia Scientific, Inc., 2700 Richards Road, Bellevue, WA 98005, USA. (yogi@sequoiasci.com)

A. Whitmire, College of Oceanic and Atmospheric Sciences, Oregon State University, 104 Ocean Administration Building, Corvallis, OR 97331, USA.